Research Square

Preprints are preliminary reports that have not undergone peer review.
They should not be considered conclusive, used to inform clinical practice,
or referenced by the media as validated information.

Allometric scaling of resting-state EEG network topography across childhood and adolescence

Xiangzhu Li
Shenzhen Hospital of Integrated Traditional Chinese and Western Medicine
Huang Tan
University of Electronic Science and Technology of China
Guangmou Cai
Shenzhen Hospital of Integrated Traditional Chinese and Western Medicine
Rui Zhang
Shenzhen Hospital of Integrated Traditional Chinese and Western Medicine
Qin Zhang
Shenzhen Hospital of Integrated Traditional Chinese and Western Medicine
Haojian Mai
Shenzhen Hospital of Integrated Traditional Chinese and Western Medicine
Qihui Zhang
Shenzhen Hospital of Integrated Traditional Chinese and Western Medicine
Gaozhan Xie
Nanjing University of Posts and Telecommunications
Li Zhang
zhanglith@163.com

Shenzhen Hospital of Integrated Traditional Chinese and Western Medicine

Research Article

Keywords: EEG, functional brain networks, developmental allometry, graph theory, childhood and adolescence, Healthy Brain Network

Posted Date: November 12th, 2026

DOI: https://doi.org/10.21203/rs.3.rs-11544154/v1

License: This work is licensed under a Creative Commons Attribution 4.0 International License.
Read Full License

Additional Declarations: No competing interests reported.

Allometric scaling of resting-state EEG network topography across childhood and adolescence

Xiangzhu Li[1,2], Huang Tan[3], Guangmou Cai[1,2], Rui Zhang[1,2], Qin Zhang[1,2], Haojian Mai[1,2], Qihui Zhang[1,2], Gaozhan Xie[4,*], Li Zhang[1,2,*]

[1] Shenzhen Hospital of Integrated Traditional Chinese and Western Medicine, Shenzhen, Guangdong, China.

[2] Shenzhen Clinical College of Integrated Chinese and Western Medicine, Guangzhou University of Chinese Medicine, Shenzhen, Guangdong, China.

[3] University of Electronic Science and Technology of China, Chengdu, Sichuan, China.

[4] State Key Laboratory of Flexible Electronics (LoFE) & Institute of Advanced Materials (IAM), Nanjing University of Posts and Telecommunications, Wenyuan Road, Nanjing, China.

[*]Corresponding authors: Gaozhan Xie (iamgzxie@njupt.edu.cn); Li Zhang (zhanglith@163.com).

Abstract. Brain network topography undergoes complex reorganization throughout childhood and adolescence. Quantifying the functional form of this maturation remains a key challenge. Here, we applied developmental allometry to sensor-level resting-state EEG networks from 1,957 participants aged 5–21 years (Healthy Brain Network). We fitted power laws of age to four graph-theoretic indices (small-worldness, global and local efficiency, modularity) across five frequency bands. Nineteen of the 20 band-by-index exponents were negative. Low-frequency (delta and theta) small-worldness showed the steepest declines (alpha = -0.878 and -0.868), indicating a near-halving of the metric with each doubling of age. Lobe-resolved analyses revealed a pan-lobar but non-uniform decline, with posterior regions showing steeper age-related changes than frontal regions in specific bands. While raw-space cross-validation did not uniquely favor the power law over linear models, its scale-free exponent provides a unified parameter to compare developmental rates across spatial and spectral scales. Individual deviations from this topology did not track dimensional psychopathology. These exponents provide a quantitative reference for EEG network topography maturation and highlight the necessity of frequency- and region-specific modeling.

Keywords: EEG; functional brain networks; developmental allometry; graph theory; childhood and adolescence; Healthy Brain Network

1. Introduction

Childhood and adolescence are periods of extended cortical reorganization (Gogtay et al. 2004; Casey et al. 2008), and a quantitative description of this reorganization is a prerequisite for both quantitative charting of typical development and the identification of deviations linked to psychiatric symptomatology. Resting-state electroencephalography (EEG) offers the millisecond

resolution and scalable acquisition needed for pediatric cohorts and has become a primary tool for population-scale developmental neuroimaging.

Graph-theoretic indices summarize functional brain networks with a small set of interpretable scalars. Global efficiency, local efficiency, modularity, and small-worldness have each proven sensitive to development and psychopathology (Bullmore and Sporns 2009; Rubinov and Sporns 2010). What has rarely been asked is whether their *form* of change with age is itself a characterizing property of development. In biology, power-law scaling between form and size, known as allometry, has long served as such a unifying descriptor (Huxley 1932; West et al. 1997). When the size variable is chronological age rather than body mass, the framework is known as developmental allometry: the exponent α quantifies the proportional change of a trait per multiplicative change in age. Applied to a topological index y and age, the model

$$\log y = \alpha \log \text{age} + \log k$$

collapses an entire developmental trajectory into two interpretable parameters and yields a residual that flags individual outliers. Allometric formulations have been informative for cortical structure and connectome development (Zhang and Sejnowski 2000; Vértès and Bullmore 2015), but EEG applications have been limited by sample size. We used the power law as a descriptive summary rather than a mechanistic model. A good log-log fit indicates scale-invariance of a trajectory, not a particular cellular process, so the interpretive weight of the work lies in the exponent estimates themselves.

The Healthy Brain Network (HBN) (Alexander et al. 2017; Shirazi et al. 2024) now provides more than 2,000 high-density resting-state EEG recordings spanning childhood and adolescence. This scale enables not only a global allometric test but also a lobe-resolved one. The latter is motivated by the reported regional gradient in which primary sensory cortices (occipital, temporal) tend to mature earlier than association and prefrontal regions (Gogtay et al. 2004; Whitford et al. 2007; Gao et al. 2017).

The present study addressed four questions. First, do EEG topological indices follow a power-law relation with age across five canonical frequency bands? Second, what are the magnitudes and significances of the resulting exponents? Third, does the exponent vary across cortical lobes, and does this frequency × region interaction reveal a regionally specific age-associated trajectory? Fourth, do deviations from the fitted trajectory track dimensional psychopathology on the Child Behavior Checklist (CBCL) (Achenbach and Rescorla 2001), which captures the distributed, transdiagnostic nature of child and adolescent psychopathology (Insel and Cuthbert 2009; Caspi and Moffitt 2018)? By answering these, we aim to characterize the topological scaling laws of pediatric EEG networks and provide a methodological benchmark for future topography studies.

2.Materials and methods

2.1 Participants

We analyzed resting-state EEG from the Healthy Brain Network (HBN) project (Alexander et al. 2017; Shirazi et al. 2024), combining ten publicly released datasets corresponding to Releases 1–10 (OpenNeuro ds005505–ds005512, ds005514, and ds005515). Release 11 (ds005516) was not included. All ten releases were processed with the identical preprocessing and network-

construction pipeline described below, and release identity was included as a covariate in robustness analyses (**Section 3.6**). Of the 2,480 participants with available phenotypic records and a resting-state session, 2,471 recordings could be audited and 1,967 of these (79.6%) passed quality control (QC). A further ten participants whose networks were numerically degenerate under the primary criterion (Section 2.4) were removed, leaving 1,957 for the primary analyses. Participants in the primary sample were 5–21 years of age (mean 9.9±3.2 years) and 32.7% were female. The age distribution was skewed towards middle childhood: 646 aged 5–7 years (33.0%), 692 aged 8–10 (35.4%), 380 aged 11–13 (19.4%), 180 aged 14–16 (9.2%) and 59 aged 17–21 (3.0%); 340 participants (17.4%) were 13 years or older. Per-release composition and audit pass rates are given in Table S5, and participants retained versus excluded by QC are compared in Table S5b. Phenotypic variables included age, sex, Edinburgh Handedness Questionnaire (EHQ) total, and CBCL bifactor scores (p-factor, attention, internalizing, externalizing).

2.2 EEG acquisition and preprocessing

EEG was recorded at 500 Hz using a Geodesic HydroCel system of 128 electrodes plus the Cz reference electrode, i.e. 129 physical channels (impedance <40 kΩ). Signals were acquired with the Cz reference; the Cz channel was then discarded before network construction, so all graphs contain 128 nodes (**Section 2.5**). No average-reference or source-referencing re-transformation was applied, and no ICA or artifact-subspace rejection was performed; artifact handling relied on the channel-level amplitude audit and the channel count rule described below (**Section 4.5**). Resting-state segments comprised eyes-open and eyes-closed periods. Eyes-closed segments were extracted from explicit event annotations where available. Where no such annotation existed, we ranked non-overlapping 40-s windows by alpha (8–13 Hz) power and used the one or two highest-power windows as proxy eyes-closed intervals. An audit of the annotations across the 1,967 QC-passed recordings found that 1,962 (99.7%) carried explicit eyes-closed event markers ("instructed_toCloseEyes"). The alpha-power proxy was therefore used for only 5 subjects.

A 2-s margin was trimmed from the start of each selected segment, leaving 38s for analysis. Signals were band-pass filtered (0.5–45 Hz) and 60 Hz notch filtered, after which the Cz reference channel was removed. Bad channels were identified with a robust amplitude criterion: a channel was flagged when its across-time standard deviation exceeded the cross-channel median by more than three robust standard deviations. Flagged channels were then interpolated from neighbouring sensors. When more than 30% of channels were flagged, no interpolation was applied.

We acknowledge that sensor-level EEG topography is inherently subject to volume conduction and reference effects. However, source localization across ten heterogeneous releases introduces distinct inverse-model assumptions that would hinder cross-cohort standardization. Therefore, we focused on sensor-space topology using absolute correlation-based connectivity, which is robust to reference choice and largely insensitive to volume conduction when proportional density thresholding is applied (Ledoit and Wolf 2004; Power et al. 2011).

2.3 Network construction

For each frequency band (δ: 0.5–4 Hz; θ: 4–8 Hz; α: 8–13 Hz; β: 13–30 Hz; γ: 30–45 Hz), data were segmented into 2-s windows with 50% overlap. Ledoit-Wolf regularized covariance

matrices were estimated per window and aggregated via log-Euclidean (Riemannian) mean (Ledoit and Wolf 2004); the pooled covariance **C** was then converted to a correlation matrix, $R_{ij}=C_{ij}/\sqrt{C_{ii}C_{jj}}$, whose off-diagonal entries served as functional-connectivity estimates. Adjacency matrices were constructed by proportional density thresholding: the 20% of node pairs with the largest absolute correlation magnitude were retained, and each retained edge carried its signed correlation weight. This density threshold balances graph connectedness with sparse topology and follows common practice in developmental EEG network studies (Opsahl et al. 2010; Power et al. 2011). The sliding-window approach was used solely to estimate a robust, artifact-resistant covariance matrix via the Riemannian center of mass. It yielded a single static connectivity matrix per subject for the subsequent allometric analysis. A schematic of the full construction pipeline and of the four graph-theoretic indices is provided in **Figure 1** and Supplementary **Figure S1**.

To verify that the choice of a 20% density threshold did not drive the observed negative allometric scaling, we re-estimated α at five density thresholds (10%, 15%, 20%, 25%, 30%; **Section 3.4**). These were applied to the two strongest-scaling indicators, global efficiency and small-worldness, in the delta and theta bands. The allometric exponent remained significantly negative across the full range in all four band×metric combinations of the primary sample (largest FDR-corrected $q=9.9\times10^{-46}$), confirming that the reported age-related decline is robust to the threshold choice.

2.4 Primary sample and degenerate networks

Fixed-density thresholding can leave a subject with a numerically degenerate network. After channel interpolation and the more-than-30%-flagged rule, a handful of recordings yield thresholded graphs that are effectively disconnected in one or more bands, so that efficiency-type indices collapse to values of order 10^{-16} and σ collapses with them. These are measurement failures rather than observations of a genuinely sparse network. Because the allometric model is fitted in logarithms, a value of 10^{-16} sits at $\log(10^{-16})\approx-36.8$. Depending on the index this is 14 to 44 standard deviations below the mean, so such values carry very large leverage.

We therefore made the exclusion of such recordings the primary analysis rather than a robustness check. The criterion was defined on the empirical distribution and not on the fitted exponents: an observation was called degenerate when its value fell below 10^{-12}. Within each affected index the degenerate values form an isolated cluster. The smallest non-degenerate value of that index lies 6.7 to 10.9 orders of magnitude above it, so the threshold never dissects the bulk of a distribution. Only the modularity indices, which never go numerically degenerate, take values near the cut; these belong to the same ten subjects and are removed with them. Ten recordings, 0.51% of the sample, were degenerate in at least one of the 20 global band-by-index fits (110 flagged observations in total). Subjects were dropped as units, so all of their global and lobe-resolved observations were removed, leaving a primary sample of n=1,957. The same rule and the same threshold were applied to every analysis in this paper, including the model comparison, the lobe-resolved fits, the interaction tests and the clinical associations.

Excluding subjects on a numerical criterion requires demonstrating that the result does not depend on it. We therefore re-estimated all 20 global models on the full 1,967-recording sample (**Table S2**) and report standard influence and residual diagnostics for the primary fits, namely

maximum Cook's D, the number of observations exceeding $4/n$, maximum leverage, and residual skew and kurtosis (**Table S3**). The two samples agree in sign and rank order; the median absolute shift of α was 0.10 and the largest was 0.21, and the only sign change (beta-band σ) occurred in a fit that was non-significant in both samples. Removing the degenerate observations mainly sharpens the estimates: for delta-band E_{glob} the 95% interval narrows from [−0.950, −0.403] to [−0.628, −0.524].

2.5 Lobe assignment

The 128 retained electrodes were assigned to one of five canonical lobes following the Geodesic HydroCel sensor layout: frontal (42 electrodes), occipital (32), central (23), parietal (19) and temporal (12), summing to the 128 graph nodes. For each lobe we extracted the corresponding sub-matrix from the full 128×128 adjacency matrix and re-computed the topological indices on this lobe-specific sub-network. Lobe assignment was performed prior to graph-theoretic computation, ensuring that all four indices were estimated on lobe-restricted connectivity rather than on summary statistics of the global network.

2.6 Graph-theoretic indices

Four indices were computed for every subject in every band（**Figure. S1**）:

- ***Global efficiency*** **(E_{glob})**: the average inverse shortest weighted path length across all node pairs, $E_{glob}=\frac{1}{n(n-1)}\sum_{i\neq j} d_{ij}^{-1}$, where the weighted distance d_{ij} is the path of minimum accumulated edge length $1/|w|$. Following the routing-efficiency formulation of Latora and Marchiori (2001), this index quantifies the capacity of the network to support parallel information transfer.

- ***Local efficiency*** **(E_{loc})**: the mean E_{glob} computed on the neighbourhood of each node, which indexes fault-tolerant modular processing (Latora and Marchiori 2001).

- ***Modularity*** **(Q)**: the Newman–Girvan modularity statistic, $Q=\frac{1}{2m}\sum_{ij}(w_{ij}-\frac{s_i s_j}{2m})\delta(c_i,c_j)$, evaluated for the partition returned by greedy modularity maximization (Newman and Girvan 2004); it captures the degree to which the network decomposes into densely intra-connected, sparsely inter-connected communities. Because modularity can be zero or negative when the greedy partition finds no community structure stronger than the degree-expected baseline, and because the allometric model is defined only for $Q>0$, modularity values ≤ 0 were treated as missing for the corresponding fit rather than transformed. The same $y>0$ requirement applies to the other three indices, which is why the effective sample size varies between lobes (**Table S4**) and, in the threshold-sweep analysis, between fit specifications (**Table 2**).

- ***Small-worldness*** **(σ)**: a weighted extension of the Humphries–Gurney ratio (Maslov and Sneppen 2002; Saramäki et al. 2007; Humphries and Gurney 2008). The index is $\sigma=(C/C_{rand})/(L/L_{rand})$, where C is the Onnela weighted clustering coefficient and L is the characteristic weighted path length (mean shortest path under the $d_{ij}=1/|w_{ij}|$ mapping) of the observed graph. C_{rand} and L_{rand} are the matched quantities averaged over degree- and strength-preserving Maslov–Sneppen rewired null models, with 20 realizations per

subject. We treat σ as a *relative* index of the local-clustering versus global-integration balance, not as an absolute classifier. Because all four constituent quantities are computed on weighted graphs, the conventional binary-network $\sigma>1$ small-world threshold does not directly transfer. We therefore draw no binary small-world classification from it.

Edge weights are absolute correlation magnitudes for all topological computations. Thresholding ranks node pairs by $|r|$ while retaining the signed correlation, and the graph metrics then operate on $|w|$ (with $d=1/|w|$ for path-based measures). Positive and negative functional coupling therefore contribute equally, and the resulting graphs are unsigned. Following the literature on developmental EEG networks, we treat E_{glob} as an integration index, E_{loc} and Q as segregation indices, and σ as a summary of the local-clustering / global-integration balance (Bullmore and Sporns 2009; Rubinov and Sporns 2010).

2.7 Allometric modeling

Population allometric exponents α were estimated by ordinary least-squares regression of $\log y$ on $\log \text{age}$, with age>0 and $y>0$. The *individual allometric deviation* (IAD) for subject i is the residual $\text{IAD}_i = \log y_i - (\hat{\alpha} \log \text{age}_i + \log \hat{k})$. The same model was fitted for both global (full 128-channel) and lobe-restricted networks. Globally, all four topological indices were fitted in each of the five bands, giving 20 global fits. At lobe level, global efficiency and small-worldness were fitted for five lobes in five bands, giving $2\times5\times5=50$ lobe-resolved fits. FDR correction was applied jointly across the 50 lobe-resolved fits (Benjamini and Hochberg 1995). All fits used the primary sample of **Section 2.4**.

Two properties of this estimator bear on interpretation. First, α is a log-scale slope obtained after linearization, not a curvature-corrected raw-scale exponent, so its confidence interval and p value rest on the usual asymptotic argument applied to log-residuals rather than on a distributional assumption about y itself; the residual diagnostics in Table S3 quantify how far the log-residuals depart from symmetry. Second, the model is defined only where $y>0$, which is why the effective sample size differs slightly across bands, indices and lobes.

To verify that the two-parameter power law is an adequate functional form rather than an arbitrary choice, each of the 20 global fits was compared with four alternatives: a linear model and a quadratic model in raw space, and a quadratic in $\log_{10}(\text{age})$ plus a penalized cubic-regression-spline generalized additive model with four basis degrees of freedom in log space. Models were compared by AIC and BIC and by five-fold cross-validated root-mean-square error, with identical folds and random seed for every specification. Three cautions apply. Information criteria are computed from likelihoods whose outcome has different units in the two spaces, so AIC and BIC are comparable only within a block and never between the raw-space and log-space blocks. Cross-validated error was therefore scored in both spaces, and we treat the raw-space comparison as the decisive one because it is the only one in which all five specifications predict the same quantity. Finally, $\log_{10}(\text{age})$ is a mild monotone reshaping of raw age over the 5–21 year window, so raw-space and log-space specifications of equal flexibility can describe almost the same family of curves, and model preference can shift with the scoring space rather than with the data. Table S1a reports the information criteria and Table S1b the cross-validated errors for all 100 model-by-fit comparisons.

2.8 Clinical associations

The clinical analysis was confined to the individual allometric deviation of global efficiency. Global efficiency is the index most directly tied to integration, it is positive for every retained subject, and restricting the planned family to one index keeps the multiplicity correction interpretable. IADs for global efficiency existed in each of the five bands and entered partial Spearman correlations with four CBCL outcomes (p-factor, attention problems, internalizing problems, externalizing problems), controlling for sex *and* age, because the allometric residual removes only the sample-average trend and can still co-vary with age within a band. This defined a planned family of 5×4=20 tests corrected by Benjamini–Hochberg FDR (Benjamini and Hochberg 1995) (**Table S6**). An exploratory analysis repeated the same procedure for all 20 band × index combinations, a family of 20×4=80 tests with its own correction, and is reported as hypothesis-generating only (**Table S6b**). ROC analysis evaluated IAD discrimination of elevated externalizing problems, with cases defined as a CBCL externalizing score more than one standard deviation above the sample mean (n=211 of the 1,939 participants contributing to the planned family), and bootstrap confidence intervals for the area under the curve.

3.Results

3.1 Developmental allometry of EEG networks

All 20 frequency-band×topological-index fits returned an estimable exponent in the primary sample, and 19 of the 20 were negative ($\alpha \in [-0.878, +0.059]$, **Table 1**), meaning that almost every index declined with age in a power-law fashion. The steepest effects were concentrated in the low-frequency bands for small-worldness and for both efficiency indices, and the flattest in the beta band (**Figure 2**). **Table 1** reports the full set of estimates with 95% confidence intervals, the prefactor k, and Benjamini–Hochberg q values for the 20-test family; the six steepest exponents run from −0.878 (delta-band small-worldness) to −0.564 (delta-band local efficiency). After correction, 15 of the 20 exponents remained significant at $q<0.05$. The five exceptions were modularity in the delta band, small-worldness in the gamma band, and the beta-band values for small-worldness and the two efficiency indices, none of whose intervals excluded zero. Explained variance was modest in absolute terms but several times larger than in the unfiltered analysis (R^2 from 0.02% to 25.3%), because the degenerate observations had dominated the residual variance. These exponents still describe a direction and rank order of age-related change rather than a strong single-variable predictor.

Model comparison treated the power law as a hypothesis to be tested rather than an assumption. Five specifications were compared for each of the 20 global fits: a linear model and a quadratic model in raw space, and the power law, a log-quadratic, and a spline GAM in log space. AIC, BIC, and five-fold cross-validated RMSE were computed for all of them, in both scoring spaces (**Tables S1a** and **S1b**). The outcome depended on the scoring space, and none of the comparisons favored the power law unambiguously.

In raw space, where all five specifications predict the same quantity, cross-validation selected the linear model for 11 of the 20 fits and the quadratic for the remaining 9. The power law was never the best raw-space predictor. In log space the ranking shifted: the spline GAM was preferred for 10 fits, the log-quadratic for 6, and the power law for 4, with the log-quadratic and the GAM

each attaining lower log-space error than the power law for 15 of the 20 fits. Among the log-space information criteria, which are mutually comparable but not comparable to raw-space ones, the log-quadratic minimized AIC for 15 fits and BIC for 13, the power law for 1 and 7 respectively, and the GAM for the remaining 4 under AIC.

To evaluate the functional form, the power law was compared with raw-space linear and quadratic models, and log-space quadratic and GAM models. While raw-space cross-validation slightly favored linear and quadratic fits, the predictive differences were negligible. We retained the power law not as a uniquely superior predictive model, but because its exponent (alpha) provides a dimensionless scaling parameter. In the context of network topography, alpha offers a direct index of proportional reorganization, enabling comparison across frequency bands and spatial subnetworks, which is mathematically unattainable with raw polynomial coefficients.

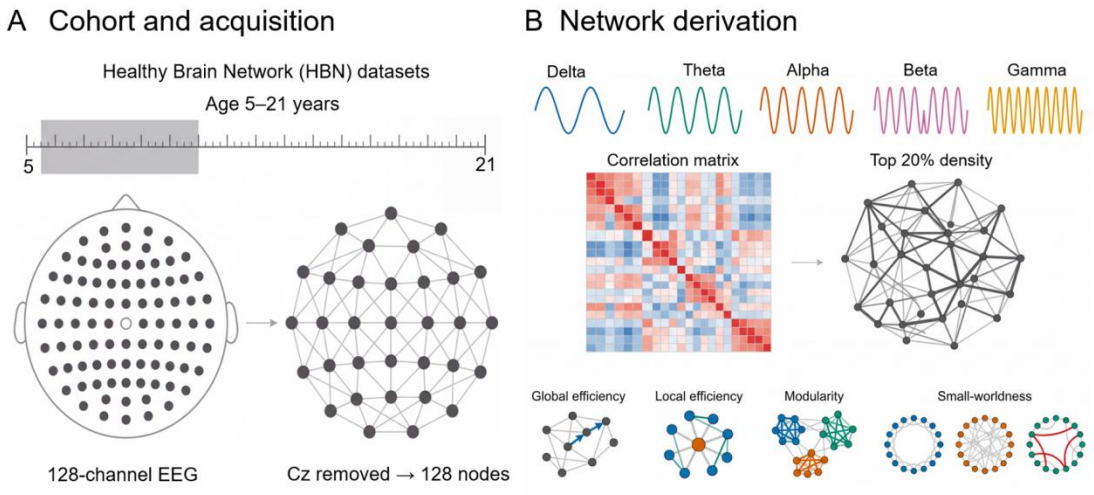
The raw-space linear and quadratic fits were near-identical in predictive accuracy. We therefore do not read the raw-space preference for a linear form as evidence against a monotonic developmental trajectory. Within the narrow age range covered by the sample, linear, quadratic and power-law forms are simply difficult to separate, and $\log_{10}(\text{age})$ is only a mild reshaping of age. We accordingly retain the power law for its interpretability rather than its fit. It is the only form in which the developmental trajectory collapses to a single scale-free exponent that can be compared across bands, indices and lobes. Among the evaluated specifications it is a parsimonious descriptive summary, and we do not claim it to be the uniquely best or the mechanistically correct one.

Table 1. Complete statistics for the 20 global allometric fits (5 frequency bands × 4 network indices) in the primary sample of n=1,957 *participants (**Section 2.4**). Each index was modeled as* $y=k\cdot\text{age}^{\alpha}$*; α is the allometric exponent, k the prefactor, and the 95% confidence interval is the slope estimate* ±1.96 *times its standard error.* R^2 *is the coefficient of determination in log-log space, reported as a percentage. q is the Benjamini–Hochberg FDR-adjusted p value within this 20-test family. Fifteen exponents are bolded: those significant at q*<0.05 *whose intervals do not include zero. For the remaining five the intervals span zero or reach it within rounding, and one of them, beta-band small-worldness, is positive. The six steepest exponents, all in the low-frequency bands, are* **−0.878** *(delta/σ),* **−0.868** *(theta/σ),* **−0.684** *(theta/*E_{glob}*),* **−0.671** *(theta/*E_{loc}*),* **−0.576** *(delta/*E_{glob}*) and* **−0.564** *(delta/*E_{loc}*).*

Band	Index	*n*	*α*	*k*	95% CI	R^2	*p*	q_{FDR}
δ	*σ*	1,957	**−0.878**	2.380	[−0.973,−0.783]	14.3%	1.3×10^{-67}	5.0×10^{-67}
δ	E_{glob}	1,957	**−0.576**	0.849	[−0.628,−0.524]	19.6%	1.2×10^{-94}	1.2×10^{-93}
δ	E_{loc}	1,957	**−0.564**	1.340	[−0.607,−0.521]	25.3%	4.0×10^{-126}	8.1×10^{-125}
δ	*Q*	1,957	−0.036	0.338	[−0.080,0.008]	0.13%	0.106	0.13
θ	*σ*	1,957	**−0.868**	1.374	[−0.975,−0.761]	11.4%	2.3×10^{-53}	7.7×10^{-53}
θ	E_{glob}	1,957	**−0.684**	0.672	[−0.753,−0.615]	16.1%	1.6×10^{-76}	8.2×10^{-76}
θ	E_{loc}	1,957	**−0.671**	1.011	[−0.731,−0.610]	19.4%	1.1×10^{-93}	7.4×10^{-93}
θ	*Q*	1,957	**−0.152**	0.370	[−0.196,−0.109]	2.4%	7.3×10^{-12}	1.5×10^{-11}
α	*σ*	1,957	**−0.209**	0.235	[−0.325,−0.094]	0.64%	4.0×10^{-4}	5.3×10^{-4}

Band	Index	n	α	k	95% CI	R^2	p	q_{FDR}
α	E_{glob}	1,957	**−0.183**	0.187	[−0.267,−0.099]	0.92%	2.1×10^{-5}	3.2×10^{-5}
α	E_{loc}	1,957	**−0.161**	0.274	[−0.238,−0.085]	0.87%	3.7×10^{-5}	5.3×10^{-5}
α	Q	1,957	**−0.120**	0.318	[−0.168,−0.072]	1.2%	1.2×10^{-6}	2.0×10^{-6}
β	σ	1,957	0.059	0.053	[−0.064,0.182]	0.05%	0.346	0.38
β	E_{glob}	1,957	−0.023	0.059	[−0.098,0.053]	0.02%	0.554	0.55
β	E_{loc}	1,957	−0.028	0.097	[−0.096,0.040]	0.03%	0.416	0.44
β	Q	1,957	**−0.115**	0.374	[−0.155,−0.075]	1.6%	2.1×10^{-8}	3.8×10^{-8}
γ	σ	1,957	−0.118	0.016	[−0.264,0.029]	0.13%	0.117	0.14
γ	E_{glob}	1,957	**−0.333**	0.031	[−0.419,−0.246]	2.8%	9.2×10^{-14}	2.3×10^{-13}
γ	E_{loc}	1,957	**−0.309**	0.053	[−0.392,−0.227]	2.7%	2.8×10^{-13}	6.3×10^{-13}
γ	Q	1,957	**−0.162**	0.525	[−0.193,−0.130]	4.9%	5.1×10^{-23}	1.5×10^{-22}

The $\alpha\approx-0.9$ exponents for low-frequency small-worldness imply an approximate rate: across a doubling of age the metric falls to about $2^{-0.88}\approx0.54$ of its previous value. The ratio σ compares weighted clustering to weighted path length, each normalized to its degree- and strength-matched null. A near-−1 exponent is therefore consistent with this relative local-clustering and global-integration balance shifting proportionally across the age range spanned by the sample. The model has no inflection point by construction. The data, however, do not distinguish a strict power law from a linear or quadratic decline over a range this narrow. The exponent should therefore be read as a coarse summary of the rate rather than a precise allometric constant.



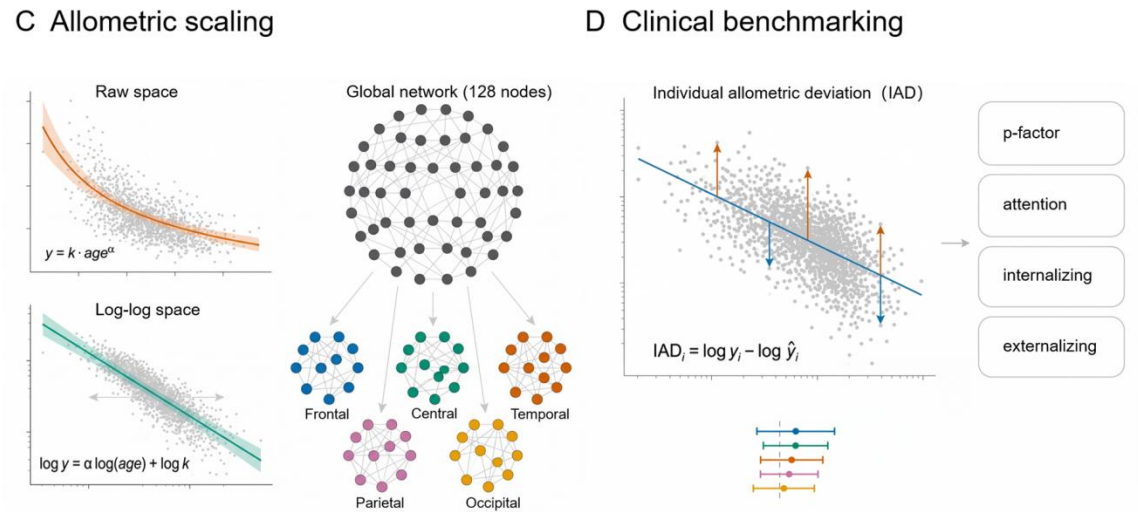


Figure 1. *Conceptual framework and analytical workflow of resting-state EEG network allometry across childhood and adolescence.* ***(A) Cohort and acquisition.*** *The cohort comprises 1,957 participants (aged 5–21 years, mean* 9.9±3.2 *years, 32.7% female) from ten publicly released Healthy Brain Network (HBN) datasets, retained after quality control. Resting-state EEG was recorded with a 128-channel Geodesic HydroCel montage; the Cz reference was discarded, yielding 128 graph nodes.* ***(B) Network derivation and parameterization.*** *Signals are decomposed into five bands, δ (0.5–4 Hz), θ (4–8 Hz), α (8–13 Hz), β (13–30 Hz), and γ (30–45 Hz). Sliding-window covariance matrices are pooled via Riemannian geometry and thresholded to the top 20% strongest connections, then summarized by global efficiency (E_{glob}), local efficiency (E_{loc}), modularity (Q), and small-worldness (σ).* ***(C) Allometric scaling.*** *Each metric y follows* $y=k\cdot \text{age}^{\alpha}$, *linearized as* $\log y = \alpha \log(\text{age}) + \log k$, *where* $\alpha<0$ *indicates developmental decline. Models are fit globally (128 channels; 20 fits) and within five lobes (frontal [42], central [23], temporal [12], parietal [19], occipital [32]; 50 fits).* ***(D) Clinical benchmarking.*** *The individual allometric deviation (*$\text{IAD}_i = \log y_i - \log \hat{y}_i$*) measures the vertical residual from the fitted log–log trajectory and is tested against Child Behavior Checklist (CBCL) dimensions (p-factor, attention, internalizing, externalizing) to assess symptom burden against a normative trajectory. Panels A–D are schematic illustrations, not empirical data plots.*

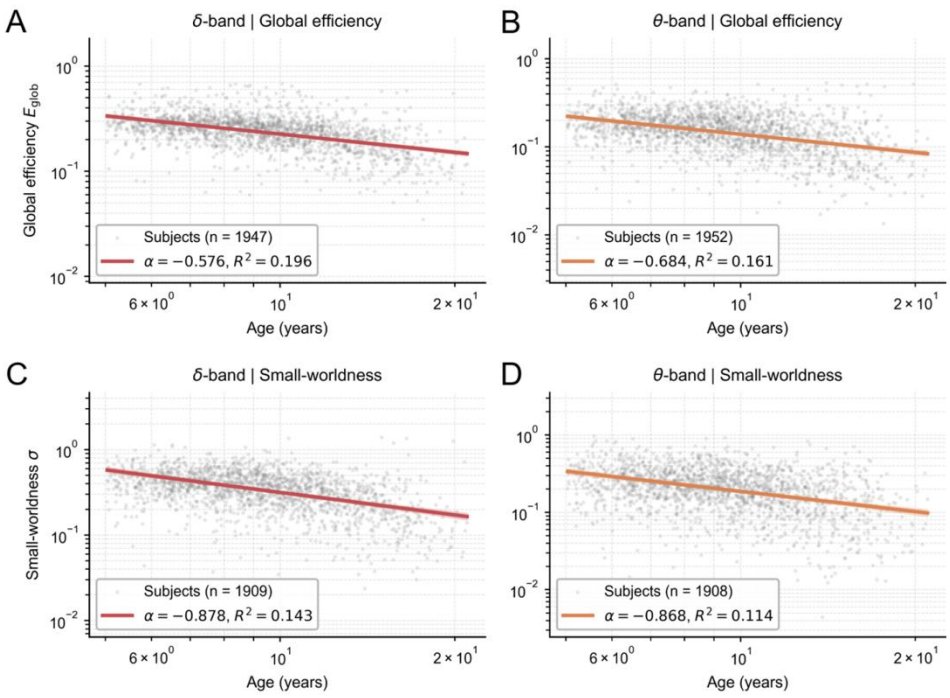


Figure 2*. Allometric scaling of EEG network indices across development in log-log space, for the primary sample of* 1,957 *participants. Each panel shows individual subjects (grey dots) overlaid with the OLS regression line (solid) and its 95% confidence interval (shaded band). The strongest age-related declines are observed in the theta and delta bands for both global efficiency (E_{glob}) **(A,B)**and small-worldness (σ)**(C,D)**; slopes close to −1 correspond to a roughly halving of these metrics across each doubling of age. The ten subjects whose thresholded networks were numerically degenerate for one or more indices (**Section 2.4**) are excluded from both the plotted points and the fitted lines; retaining them tilted the low-frequency fits and inflated the intervals without changing the sign of any exponent.*

3.2 Age-stratified distributions

Figure 3A illustrates the continuous developmental trajectory of one of the most strongly scaling indices, theta-band global efficiency. It shows individual observations, age-bin means with 95% confidence intervals, and the fitted power-law prediction.

3.3 Clinical associations

In the primary sample, 1,939 participants had both a usable IAD and CBCL ratings, and no association in the planned family of 20 tests reached significance after FDR correction (smallest p=0.040, corresponding q=0.469; **Table S6**). The strongest of these pointed in a consistent direction, with larger (less negative) gamma-band efficiency IAD relating to more externalizing (r=+0.047) and attention problems (r=+0.042), but both were uninterpretable once corrected. The exploratory extension to all 20 band × index IADs, a family of 80 tests, was equally null: four associations reached unadjusted p<0.05, the smallest corrected q was 0.741, and none survived FDR control (**Table S6b**). ROC analysis of externalizing risk above +1 SD (n=211 cases, 1,728 non-cases) was at chance for every band, with areas under the curve between 0.502 (δ; 95% CI [0.435,0.570]) and 0.540 (γ; 95% CI [0.473,0.608]), all intervals covering 0.5 (**Figure 3B**).

These results bound the practical value of a single band-level allometric residual as a behavioral marker; they do not establish that network allometry is unrelated to symptom burden, because the sample was not ascertained for psychopathology and the effect sizes detectable at this size are moderate at best.

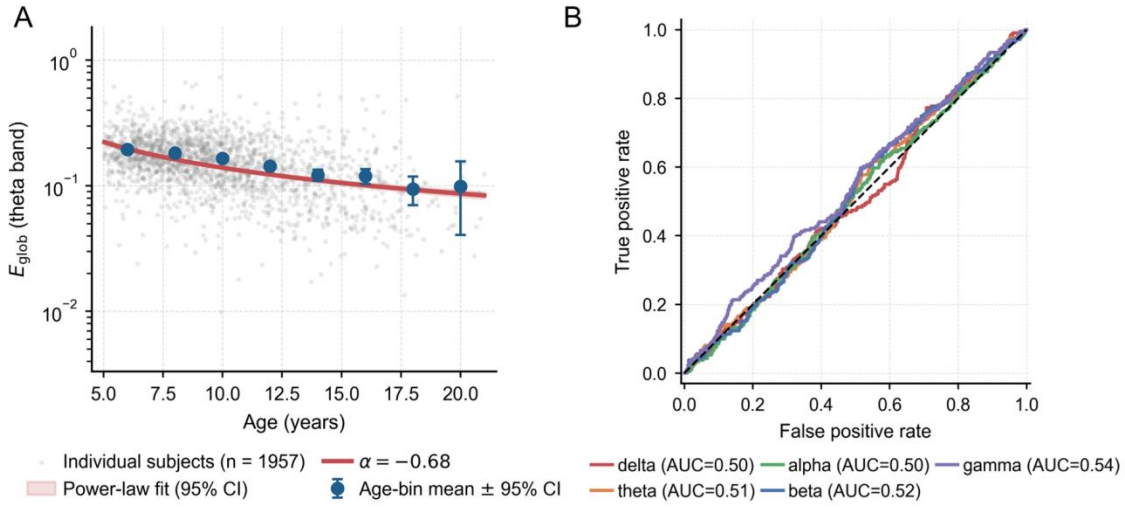


Figure 3*. Developmental trajectory of theta-band global efficiency and IAD-based discrimination of externalizing risk.*

(A) In the primary sample, theta-band global efficiency declined with age. Grey dots represent individual participants; blue markers show means with 95% confidence intervals in two-year age bins; the red line shows the fitted power-law trajectory with its 95% confidence band. The y-axis is logarithmic.

(B) ROC curves for the individual allometric deviation (IAD) of global efficiency in discriminating Child Behavior Checklist (CBCL) externalizing high-risk status, defined as a score more than one standard deviation above the sample mean (n = 211 cases and 1,728 comparison participants). Curves are shown for five frequency bands. Discrimination was close to chance: areas under the curve ranged from 0.502 to 0.540, and all 95% confidence intervals included 0.5. These results are consistent with the null partial correlations reported in the main text.

Abbreviations: IAD, individual allometric deviation; CBCL, Child Behavior Checklist; ROC, receiver operating characteristic; AUC, area under the curve.

3.4 Threshold robustness of the allometric scaling pattern

We first assessed whether the choice of a 20% density threshold materially influenced the reported scaling exponents. To this end, α was re-estimated for the two strongest-scaling indicators across five density thresholds ranging from 10% to 30% (**Table 2**, **Figure 4**), on the same primary sample as the main analysis. All 20 estimates (2 bands × 2 metrics × 5 densities; n=1,955 – 1,957 depending on metric and threshold) remained significantly negative after Benjamini–Hochberg correction (largest $q=9.9\times10^{-46}$), with α varying only modestly across the

threshold range. Three of the four combinations strengthened monotonically in magnitude as density increased: small-worldness ranged from −0.761 to −0.926 in the delta band and global efficiency from −0.517 to −0.615 (delta) and −0.617 to −0.717 (theta), whereas theta-band small-worldness was essentially flat (−0.854 to −0.868). Small-worldness exponents were consistently more negative than efficiency exponents at every threshold, consistent with the greater sensitivity of the rescaled clustering ratio to the retention of weaker short-range connections. These findings indicate that the age-related decline is not an artefact of a single arbitrary threshold choice.

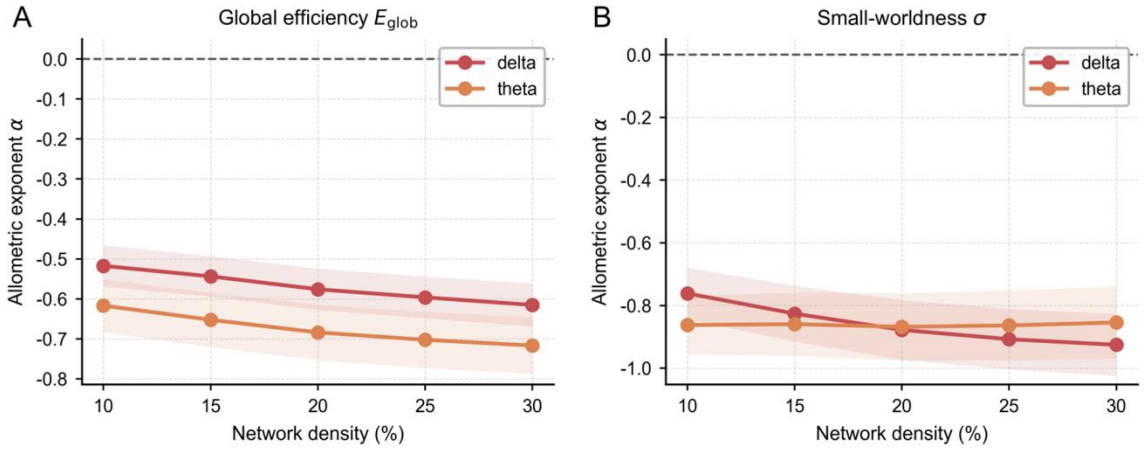


Figure 4. *Threshold robustness of allometric scaling. Allometric exponent α is plotted as a function of network density threshold (10–30%) for global efficiency (E_{glob}, left) and small-worldness (σ, right) in the delta and theta bands, on the primary sample. All α remain significantly negative across the full range (largest FDR-corrected q=9.9×10^{-46}), confirming that the reported age-related decline is robust to threshold choice. Shaded bands indicate approximate 95% confidence intervals on α .*

Table 2. *Allometric exponent α across network density thresholds (delta and theta bands), estimated on the same primary sample as the main analysis (n=1,955–1,957 per fit after subject-specific threshold validity checks; the sample size is given in the Metric column). All values remain significantly negative after Benjamini–Hochberg correction (largest q=9.9×10^{-46}). Bold values indicate q<0.05.*

Band	Metric	$\alpha_{10\%}$	$\alpha_{15\%}$	$\alpha_{20\%}$	$\alpha_{25\%}$	$\alpha_{30\%}$
δ	σ (1,956–1,957)	**−0.761**	**−0.826**	**−0.878**	**−0.907**	**−0.926**
δ	E_{glob} (1,957)	**−0.517**	**−0.544**	**−0.576**	**−0.596**	**−0.615**
θ	σ (1,955–1,957)	**−0.862**	**−0.860**	**−0.868**	**−0.864**	**−0.854**
θ	E_{glob} (1,957)	**−0.617**	**−0.652**	**−0.684**	**−0.702**	**−0.717**

3.5 Lobe-specific allometric scaling

We tested whether the allometric exponent itself varies across cortical regions. To this end, α for global efficiency and small-worldness was re-estimated within each of five lobes (frontal, central, temporal, parietal, occipital) and across all five frequency bands, on the primary sample. This yielded 50 fits (5 lobes ×5 bands ×2 indices), with n between 1,030 and 1,957 because a lobe sub-network must itself be non-degenerate to enter a fit. **Table 3** reports the exponents with their q values, and **Table S4** gives the complete fit statistics; the gamma-band pattern is illustrated in **Figure 5**, and all 50 fits are mapped in **Figure 6**. Whether the regional differences are statistically distinguishable, rather than only descriptive, was tested with a region-by-age interaction model for each of the ten band-by-index combinations (**Section 2.5**); those results are reported with the robustness analyses in **Section 3.6** and listed in **Table S7**.

Table 3. *Lobe-resolved allometric exponents α for global efficiency (E_{glob}) and small-worldness (σ) in the primary sample, per lobe and band; n ranges from* 1,030 *to* 1,957 *across the 50 fits. Values in parentheses are Benjamini–Hochberg q across the 50 tests. Bold values indicate* $q<0.05$*;* † *marks* $.05\leq q<.10$*. The only significantly positive exponent is beta-band small-worldness in frontal cortex. Full fit statistics are in* ***Table S4*** *and the interaction tests in* ***Table S7****.*

Band	Metric	Frontal	Central	Temporal	Parietal	Occipital
δ	E_{glob}	**−0.463** (4.2×10⁻	**−0.666** (3.3×10⁻	**−0.530** (1.9×10⁻	**−0.754** (1.7×10⁻	**−0.613** (8.7×10⁻
δ	σ	**−0.643** (3.3×10⁻	**−0.820** (1.9×10⁻	**−0.729** (5.4×10⁻	**−0.528** (7.3×10⁻	**−0.632** (2.4×10⁻
θ	E_{glob}	**−0.681** (2.4×10⁻	**−0.806** (4.5×10⁻	**−0.626** (1.1×10⁻	**−0.800** (2.2×10⁻	**−0.625** (3.6×10⁻
θ	σ	**−0.696** (2.8×10⁻	**−0.792** (6.3×10⁻	**−0.697** (7.9×10⁻	**−0.746** (3.7×10⁻	**−0.666** (8.1×10⁻
α	E_{glob}	**−0.183** (1.5×10⁻	**−0.304** (7.1×10⁻	**−0.208** (9.7×10⁻	**−0.172** (6.1×10⁻	**−0.103** (0.025)
α	σ	**−0.114** (0.029)	**−0.444** (7.8×10⁻	**−0.145** (0.024)	**−0.183** (3.5×10⁻	**−0.143** (0.006)
β	E_{glob}	−0.042 (0.263)	**−0.134** (0.002)	**−0.106** (0.006)	−0.086† (0.054)	0.023 (0.579)
β	σ	**0.109** (0.041)	**−0.175** (0.044)	**−0.194** (4.7×10⁻	−0.067 (0.143)	0.014 (0.760)
γ	E_{glob}	**−0.280** (7.4×10⁻	**−0.430** (3.1×10⁻	**−0.445** (2.9×10⁻	**−0.391** (1.5×10⁻	**−0.404** (6.6×10⁻
γ	σ	0.071 (0.269)	**−0.346** (1.0×10⁻	**−0.358** (3.9×10⁻	**−0.307** (4.9×10⁻	**−0.233** (4.7×10⁻

The lobe-resolved fits sharpened the global picture in three ways, and the formal region-by-age interaction tests (**Table S7**) supported two of them. Low-frequency decline was pan-lobar but not uniform. Delta- and theta-band global efficiency fell significantly in all five lobes, from −0.463 (frontal) to −0.754 (parietal) in the delta band and from −0.625 (occipital) to −0.806 (central) in the theta band. For delta-band efficiency the interaction was significant ($F=14.59$, $q=7\times10^{-11}$), and the parietal-versus-frontal contrast survived correction ($q=7.2\times10^{-8}$), so the posterior emphasis is statistically distinguishable rather than merely descriptive. Gamma-band decline was strongest in temporal cortex. The steepest efficiency exponent appeared in the temporal lobe (−0.445, $q=2.9\times10^{-22}$) and the flattest in the frontal lobe (−0.280), but the omnibus interaction for gamma-band efficiency was not significant ($q=0.142$), so this particular ordering remains

descriptive. Mid-frequency fits were weak but widespread. All ten alpha-band fits reached significance (efficiency −0.103 to −0.304; small-worldness −0.114 to −0.444), with central cortex steepest on both indices, whereas only 5 of the 10 beta-band fits were significant.

The spatial distribution of the allometric exponents revealed distinct topographic gradients (**Figure 5**, **Figure 6**). Low-frequency (delta and theta) global efficiency and small-worldness declined significantly across all five lobes, indicating a pan-lobar maturation process. However, the magnitude of this decline was not uniform. In the delta band, global efficiency declined most steeply in parietal cortex (alpha = -0.754) compared to frontal cortex (alpha = -0.463; interaction q < 0.001). In the gamma band, the steepest declines occurred in temporal cortex (alpha = -0.445 for efficiency and -0.358 for small-worldness), whereas frontal small-worldness displayed a non-significant positive trend (alpha = +0.071, q = 0.269). This frontal-to-posterior dissociation suggests a spatially heterogeneous maturation of topological segregation.

Small-worldness proved metric-dependent in the high bands. Its gamma-band decline was significant in four lobes (temporal −0.358, q=3.9×10^{-7}; central, parietal and occipital q≤4.7×10^{-6}) but absent in frontal cortex (+0.071, q=0.269), where it carried the opposite sign. That frontal-versus-posterior difference was formally supported: the omnibus interaction was significant (F=4.21, q=0.0070), with frontal differing from temporal (q=0.021) and parietal (q=0.020). Beta-band small-worldness likewise showed a significant *positive* frontal exponent (+0.109, q=0.041) against negative temporal (−0.194, q=4.7×10^{-4}) and central (−0.175, q=0.044) values (F=3.98, q=0.0079).

In total, 44 of the 50 lobe-resolved slopes were significant after FDR correction (10/10 in delta, theta and alpha, 5/10 in beta, 9/10 in gamma). The six exceptions were five beta-band fits (frontal and occipital efficiency, parietal efficiency at q=0.054, parietal and occipital small-worldness) plus gamma-band frontal small-worldness. Four of the ten omnibus interactions were significant, and 14 of the 100 pairwise lobe contrasts survived correction. Six of the 14 involved frontal cortex; the rest separated central, parietal, occipital and temporal pairs.

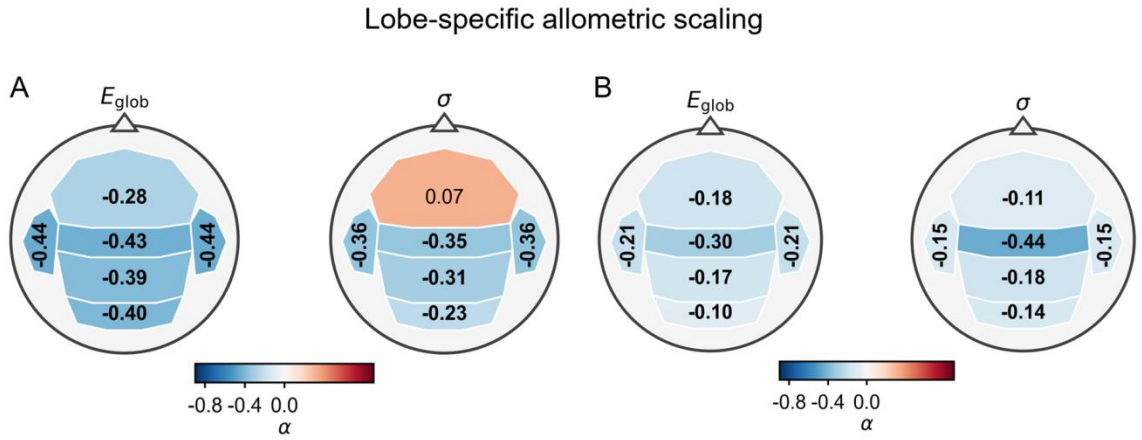


***Figure 5**. Lobe-specific allometric scaling in the gamma and alpha bands.*

***(A)** Gamma-band exponents for global efficiency (left) and small-worldness (right) across five cortical lobes (frontal, central, temporal, parietal, occipital). For global efficiency, the steepest decline was in temporal cortex (-0.445) and the flattest in frontal cortex (-0.280), but the omnibus region-by-age interaction was not significant (q = 0.142). For small-worldness, the decline was significant in temporal, central, parietal and occipital lobes, with temporal cortex steepest (-0.358). Frontal small-worldness showed a non-significant positive exponent (+0.071, q = 0.269). The frontal-versus-posterior difference was formally supported: the omnibus interaction was significant (q = 0.0070), and frontal differed from temporal (q = 0.021) and parietal (q = 0.020).*

***(B)** Alpha-band exponents for global efficiency (left) and small-worldness (right) across the same five lobes. All ten alpha-band fits were significant, with exponents ranging from -0.103 to -0.304 for global efficiency and from -0.114 to -0.444 for small-worldness. Central cortex was steepest on both indices. The region-by-age interaction was marginal for global efficiency (q = 0.052) and not significant for small-worldness (q = 0.142).*

Abbreviations: Eglob, global efficiency; sigma, small-worldness.

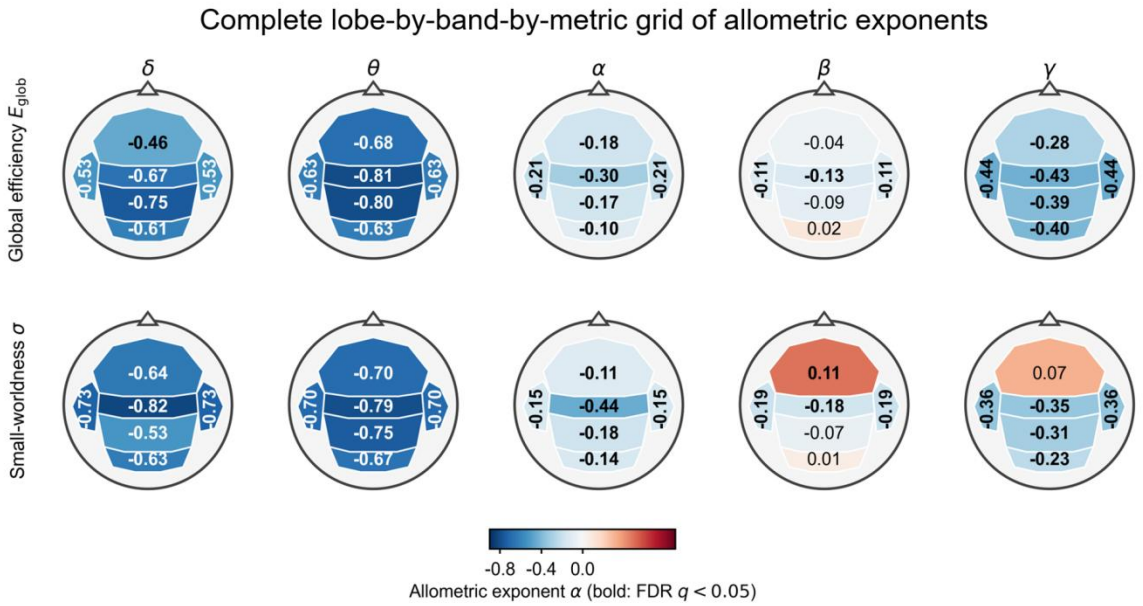


***Figure 6**. Complete lobe-by-band-by-metric grid of allometric exponents α in the primary sample. Top row: global efficiency across the five canonical frequency bands. Bottom row: small-worldness. Each schematic head encodes α for the five cortical lobes (frontal, central, temporal, parietal, occipital); darker blue indicates a more negative exponent (steeper age-related decline), and bold labels mark slopes significant after FDR correction (q<0.05). In total, 44 of the 50 slopes were significant: all delta-, theta- and alpha-band slopes, 9 of 10 in the gamma band and 5 of 10 in the beta band. The single significantly positive slope is beta-band small-worldness in frontal cortex (+0.109, q=0.041)*

3.6 Robustness of the scaling exponents

We assessed the sensitivity of the global exponents to four design factors: release composition, age-distribution balance across releases, lobe-by-age interaction, and channel selection. The first, second and fourth factors concern release composition, age balance and electrode density rather than outlier sensitivity, so those checks were run on the full sample and are reported as full-sample estimates; the interaction test follows the primary definition.

Release composition. The ten HBN releases differ in acquisition setup and cohort composition. Re-fitting each global model with release indicators included as covariates shifted the exponent only marginally ($\Delta\alpha \in [+0.015, +0.034]$ across the twenty band-by-index fits). A leave-one-release-out analysis re-estimated the delta-band global-efficiency exponent with each release removed in turn (mean $\alpha = -0.68$, range $[-0.82, -0.56]$), bracketing the full-sample estimate ($\alpha = -0.68$) and covering the primary estimate ($\alpha = -0.576$) at its lower end, so no single release drives the result.

Age-distribution balance. Because releases differ in the age range they contribute, we re-weighted the pooled sample by inverse-propensity kernel densities estimated within release, yielding an effective sample of $n \approx 492$. The largest exponent shift was −0.096 (theta-band small-worldness: α from −1.06 to −0.96), and a stratified bootstrap ($B = 1{,}000$) gave a delta-band global-efficiency interval of $[-0.89, -0.46]$ (point estimate −0.67), which also contains the primary delta-band estimate of −0.576. Release-related age imbalance therefore does not explain the power-law form.

Lobe-by-age interaction. We tested whether the age-scaling exponent differed across cortical regions. For each of the 10 band-by-index combinations, we fitted an omnibus region×log(age) interaction model with HC3 robust standard errors, giving 10 omnibus tests and 100 pairwise lobe contrasts (10 per combination). In the primary sample, 4 of the 10 omnibus tests were significant after FDR correction: delta- and theta-band global efficiency ($q = 7 \times 10^{-11}$ and $q = 1.4 \times 10^{-4}$) and beta- and gamma-band small-worldness ($q = 0.0079$ and $q = 0.0070$), with alpha- and beta-band efficiency marginal at $q = 0.052$ and $q = 0.084$. Fourteen of the 100 pairwise contrasts survived correction **(Table S7)**; six of them involved frontal cortex, and the rest separated central, parietal, occipital and temporal pairs. The regional differences described in **Section 3.5** are therefore statistically supported for four combinations and remain descriptive for the others. As before, small-worldness models used fewer complete cases ($n = 468$–917) than efficiency models ($n = 1{,}879$–$1{,}923$), which limits their power to detect interactions. In the full-sample sensitivity analysis no omnibus test approached significance (all $p \geq 0.56$; minimum $q = 0.95$), so this conclusion depends on the primary sample definition.

Node-count sensitivity. Because electrode density varies across the scalp (frontal 42, occipital 32, central 23, parietal 19, temporal 12 channels), we regressed the lobe-resolved exponents on lobe channel count using weighted least squares. The channel-count coefficient was small and non-significant ($\beta = +0.0025$, $p = 0.60$; OLS with HC3: $\beta = +0.0040$, $p = 0.30$), and the pooled exponent–channel-count correlation was weak ($\rho = 0.15$, $p = 0.31$). We found no evidence that channel count alone accounts for the regional pattern. We cannot, however, exclude that sampling density interacts with other regional properties, such as distance from the skull–electrode array or lobe-specific myelination.

4. Discussion

4.1 Global scaling as an allometric description

In the primary sample, 19 of the 20 band-by-index exponents were negative and 15 survived correction for multiple comparisons. This pattern is consistent with the broader picture that low-frequency EEG power and long-range synchronization decline with age (Whitford et al. 2007; Casey et al. 2008; Smit et al. 2011; Whitaker et al. 2016). The steepest slopes were small-worldness in the delta (−0.878) and theta (−0.868) bands; their magnitude is close to unity, so the metric falls to roughly half its value across a doubling of age, paralleling the documented trajectory of gray-matter loss through adolescence (Shaw et al. 2008). From a network topography perspective, this near-unity exponent suggests a proportional shift in the balance between local clustering and global integration. This decline aligns with the concept of economical brain organization: as the brain matures, excessive local redundancy is pruned, and functional networks become more spatially distributed and efficient (Bullmore and Sporns 2012; Vertes and Bullmore 2015). While surface EEG cannot directly measure synaptic density, this macro-scale topological contraction mirrors the micro-scale synaptic pruning and gray matter loss well-documented in structural MRI studies (Gogtay et al. 2004). Therefore, the allometric exponents derived here provide a functional counterpart to structural maturation.

The convergence across modalities (structural gray-matter contraction, low-frequency power loss, and now EEG topological allometry) is nonetheless compatible with other accounts. Because every index here correlates with EEG amplitude and density, part of this convergence could reflect shared measurement-level changes rather than distinct network properties. We therefore read the cross-modality agreement as supporting, but not establishing, a reproducible age-associated scaling phenomenon.

4.2 Lobe-specific trajectories

The lobe-resolved analysis (**Section 3.5**) clarifies what the global fits average over. Low-frequency decline was pan-lobar: delta and theta global efficiency and small-worldness were significantly negative in all five lobes. The steepest exponents were −0.754 for delta global efficiency in parietal cortex and −0.806 for theta global efficiency in central cortex. Gamma-band decline was strongest in temporal cortex (−0.445 for global efficiency and −0.358 for small-worldness) and was absent for frontal small-worldness, where the exponent was slightly positive and not distinguishable from zero (+0.071, q=0.269). For delta-band global efficiency the region-by-age interaction was significant ($q=7\times10^{-11}$) and the parietal-versus-frontal contrast survived correction ($q=7.2\times10^{-8}$), so that gradient is more than descriptive. The temporal-versus-frontal gamma ordering, by contrast, rests on an omnibus test that did not reach significance (q=0.142), and we report it as a summary of the fitted slopes rather than as an established difference.

This dissociation aligns with two strands of prior work. Structurally, posterior and temporal association cortices mature earlier than prefrontal regions (Gogtay et al. 2004; Gao et al. 2017); functionally, gamma-band oscillations subserve fine-grained stimulus-locked processing that emerges later in development (Nunez and Srinivasan 2006). The pattern is also consistent with the *last-in-first-out* hypothesis of cortical regression, in which late-maturing association areas retain the longest period of experience-dependent reorganization (Whitaker et al. 2016).

Mid-frequency effects were sparser and metric-dependent. All ten alpha-band fits reached significance, with exponents between −0.444 and −0.103, whereas only five of the ten beta-band fits did. Among those five, beta-band small-worldness in frontal cortex was significantly *positive* (+0.109, q=0.041). That is the only lobe-resolved exponent the data support as an increase with age, and it sits alongside 43 significant negative slopes, so we read it as an observation requiring replication rather than as evidence of a growing architecture. With slopes this small and confidence intervals this wide, a modest positive effect in another lobe would not have been detected.

Four of the ten omnibus interactions and 14 of the 100 pairwise contrasts survived correction (**Section 3.6**, **Table S7**). The global fits therefore do not merely average away regional structure: the gradients for delta- and theta-band global efficiency and for beta- and gamma-band small-worldness carry statistical support, with the caveat that the sigma-band interactions rest on the smaller complete-case samples (n=468 – 917) required by those fits. For the remaining combinations the descriptive ordering of lobes is not, after correction, distinguishable in slope from one another. The two-parameter ($\alpha, \log k$) summary is most interpretable when reported at the lobe level, alongside an explicit statement of the interaction test results. We therefore recommend that future allometric EEG studies report both global and lobe-resolved exponents with FDR correction across the lobe-resolved family.

4.3 Why global IADs do not track psychopathology

The lack of significant associations between the individual allometric deviation (IAD) of global efficiency and CBCL dimensions is noteworthy. It suggests that a single, spatially aggregated topological index is too coarse to capture the complex mapping between EEG network topography and psychopathology. Global efficiency collapses 128 nodes into a single scalar, discarding spatial information and frequency-specific interactions. The primary value of this work, therefore, lies not in immediate clinical translation, but in establishing a robust, quantitative developmental baseline. Future topography research should focus on region-specific IADs, multivariate network features, or microstate analyses rather than relying on single global graph metrics.

Four methodological factors plausibly attenuate the clinical signal. First, the univariate IAD aggregates over 128 channels; spatially resolved lobe-specific IADs or local efficiency deficits in frontal-striatal circuits (Whitaker et al. 2016) may be more sensitive. Second, CBCL dimensions integrate across neurobiological systems, of which macroscopic EEG topology indexes only a subset. Multivariate combinations across bands, via regularized regression or canonical correlation, may be needed to extract the shared signal (Vértès and Bullmore 2015). Third, HBN is enriched for clinical concerns (Alexander et al. 2017), attenuating the typical-vs-clinical contrast at the population level. Fourth, the cross-sectional design captures *age-correlated* features but cannot separate developmental *change* from stable *trait*; whether IADs predict symptom *trajectories* remains a question for longitudinal follow-up.

The RDoC framework (Insel and Cuthbert 2009) provides the natural motivation for quantitative developmental references of this kind: a continuous biological substrate against which the heterogeneous presentations of psychopathology can be measured (Caspi and Moffitt 2018).

4.4 Limitations

The primary sample is not age-representative of the full HBN cohort, and the attrition was not random with respect to age. Of the 2,471 recordings that could be audited, 1,967 (79.6%) passed quality control, so roughly one fifth were dropped, and the pass rate varied by release, from 88.2% in Release 1 to 72.7% in Release 10 (**Table S5**). Participants retained for the primary analysis were younger than those excluded by the audit stage (mean 9.89±3.20 versus 11.49±3.54 years; Welch $t=-9.25$, $p=2.5\times10^{-19}$; Cohen's $d=-0.49$; medians 9.29 versus 10.96, Mann–Whitney $U=362{,}400$, $p=1.1\times10^{-20}$), and their release composition also differed ($\chi^2=31.89$, $p=2.1\times10^{-4}$; **Table S5b**). Sex and CBCL scores are not available for excluded participants, so this comparison covers age and release only. The retained sample is concentrated in middle childhood, with 33% aged 5–7 and 35% aged 8–10 against 3% aged 17–21 (**Section 3.2**). Exponents therefore rest on a thin tail at the top of the age range, which lowers precision there and makes the fitted trajectory least reliable beyond about 16 years of age.

Segment selection is a far smaller concern. An audit of the available annotations found explicit eyes-closed event markers for 1,962 of the 1,967 QC-passed recordings (99.7%), so the alpha-power proxy applied to five subjects, all of them inside the primary sample. Re-fitting the 20 global models without them ($n=1{,}957\rightarrow1{,}952$) moved every exponent by at most 0.0025 (largest: γ-band local efficiency, $-0.309\rightarrow-0.307$; median 0.0006) and changed no significance verdict. The proxy procedure cannot drive the reported age-related decline.

The quantitatively larger sensitivity concerns numerically degenerate networks, and the primary analysis is defined by their removal (**Section 2.4**). Ten subjects (0.51%) returned at least one index that is zero to within floating-point precision. In delta-band small-worldness the largest of these values is 7.9×10^{-13}, while the smallest non-degenerate value of the same index is 4.4×10^{-6}, 6.7 orders of magnitude greater. These are thresholded graphs with no effective connections. Because the fits are taken in log–log coordinates, such values sit far below the data and carry very large leverage, so their exclusion is not cosmetic. **Table S2** contrasts the primary sample with the unfiltered one ($n=1{,}967$), and **Table S3** reports the influence and residual diagnostics of the primary fits.

Every exponent becomes shallower once those observations are dropped, by a median of +0.098 and a maximum of +0.210 (α-band small-worldness, $-0.420\rightarrow-0.209$). The low-frequency result survives: delta- and theta-band small-worldness remain the steepest exponents, at -0.878 and -0.868. The mid- and high-frequency exponents are the sensitive ones. Beta-band small-worldness changes sign ($-0.137\rightarrow+0.059$) while staying non-significant under both specifications, and the count of FDR-significant exponents rises from 13 of 20 in the unfiltered sample to 15 of 20 in the primary one, because the two α-band efficiency fits are attenuated by the near-zero values ($q=0.070$ and 0.10 becoming 3.2×10^{-5} and 5.3×10^{-5}). We therefore take the filtered sample as primary and the unfiltered one as the sensitivity analysis, and we confine the documented effect of the near-zero observations to the weaker mid- and high-frequency exponents rather than treating it as a threat to the low-frequency result.

4.5 Methodological limitations

Reference handling and artifact rejection were deliberately minimal. Signals were acquired against Cz, which was discarded before network construction, leaving 128 nodes; no average or

source reference was computed, and neither independent component analysis nor artifact subspace rejection was applied. Channel-level amplitude auditing and sensor interpolation did the remaining work. This keeps one pipeline identical across ten releases, at the cost of retaining reference-dependent and volume-conduction effects that a common-average or source-space comparison would attenuate.

Frequency bands were fixed a priori rather than anchored to each participant's individual alpha peak, so an age-related shift in peak frequency is absorbed into band power instead of being separated from it. Functional connectivity was assessed via static correlation. Correlation-based coupling conflates true phase synchrony with shared amplitude fluctuations, so phase-based measures such as the weighted phase-lag index, and reference-robust schemes such as the relative error difference (REST), remain to be evaluated. Dynamic sliding-window connectivity may surface transient reconfigurations that the static estimator averages away; here the windows were used only to build a robust covariance. The allometric pattern is robust across density thresholds from 10% to 30% (**Section 3.4**). Other schemes, such as MST-based thresholding and proportional-to-node-strength (Power et al. 2011), remain to be tested.

Lobe assignments followed the Geodesic HydroCel 128 layout; finer-grained parcellations (HCP-MMP1, surface-based atlases) may yield different regional gradients. Lobe-resolved fits multiply the number of statistical tests; we applied FDR across the lobe-resolved family, but stricter family-wise procedures are an alternative. The unequal channel counts across lobes also limit the statistical power of the small-worldness fits, which rest on fewer complete cases. The corresponding node-count sensitivity analysis is reported in **Section 3.6**. Finally, HBN is enriched for clinical concerns, and the present coefficients should be validated in independent cohorts before being used as general developmental reference trajectories.

5 Conclusion

In a large pediatric cohort, resting-state EEG network topography followed robust power-law scaling trajectories. By quantifying band-specific and lobe-resolved exponents, this study provides a set of reference parameters for the maturational reorganization of brain networks. While global network deviations did not track broad behavioral dimensions, these normative exponents offer a quantitative baseline for future topography studies to detect spatially localized or frequency-specific deviations in atypical neurodevelopment.

Statements and Declarations

Funding This study was supported in part by the National Natural Science Foundation of China (22105104), the Natural Science Fund for Colleges and Universities in Jiangsu Province (24KJB430030), and the Natural Science Foundation of Nanjing University of Posts and Telecommunications (NY224151).

Competing interests The authors have no competing interests to declare that are relevant to the content of this article.

Ethics approval and consent to participate This study is a secondary analysis of publicly released, de-identified data from the Healthy Brain Network (HBN) project; no new data were collected and no identifiable individual-level information was accessed. Ethical approval and

informed consent for the primary HBN study were obtained by the HBN project from its institutional review board, and all data analysed here were released by the HBN project subject to that approval. All analyses were performed on de-identified subject-level derived features.

Consent for publication Not applicable. The manuscript contains no identifiable individual information or images of human subjects.

Data availability Raw EEG data are publicly available through the OpenNeuro repository under dataset identifiers ds005505–ds005512, ds005514, and ds005515 (Releases 1–10 of HBN-EEG). The data follow the Brain Imaging Data Structure (BIDS) standard (Gorgolewski et al. 2016). Pre-processed subject-level features, allometric exponents, individual allometric deviations (IADs), partial-correlation results, and ROC results supporting the findings of this study are available at [https://github.com/fatbaby614/resting-state-EEG-Network-Topology].

Code availability All analysis code, including network construction, allometric model fitting, model comparison, and figure generation, is available at [repository URL]. The analysis was implemented in Python 3.12 using MNE-Python (Gramfort et al. 2013), networkx (Hagberg et al. 2008), scikit-learn (Pedregosa et al. 2011), scipy (Virtanen et al. 2020), and matplotlib (Hunter 2007).

Author contribution Xiangzhu Li and Li Zhang conceived and designed the study. Xiangzhu Li performed the formal analysis, developed the analysis pipeline, and wrote the original draft. Huang Tan contributed to the software development, data curation, and visualization of the results. Guangmou Cai, Rui Zhang, and Qin Zhang participated in data curation, verified the analytical outputs, and reviewed the manuscript. Mai Haojian provided methodological input and validated the statistical models. Qihui Zhang assisted with the formal analysis and cross-checked the results. Gaozhan Xie and Li Zhang supervised the project, acquired funding, and critically revised the manuscript for intellectual content. All authors read and approved the final manuscript.

Acknowledgements Data were provided by the Child Mind Institute Healthy Brain Network (Alexander et al. 2017). The authors thank the participants and their families for making this research possible.

Declaration of generative AI and AI-assisted technologies During the preparation of this manuscript, the authors used DeepSeek and ChatGPT as writing assistants to check the manuscript for language errors and to improve readability and wording. These tools were not used to generate, design, or analyse data, to run statistical analyses, or to create any figure or graphical content in the manuscript. All scientific content, methods, results, and conclusions were produced and verified by the authors, who take full responsibility for the content of the publication.

Supplementary information

Supplementary Tables S1a–S7 and Supplementary Fig. S1 are provided in the accompanying supplementary information. Supplementary Table S1a and Supplementary Table S1b report the model-comparison statistics (information criteria and cross-validated error) for all 20 global fits. Supplementary Table S2 contrasts the primary sample with the unfiltered one, and Supplementary Table S3 reports influence diagnostics. Supplementary Table S4 gives the

complete lobe-resolved fit statistics underlying the lobe-resolved results in the main text, Supplementary Table S5 reports sample composition across HBN releases, Supplementary Table S5b lists included versus excluded participants, Supplementary Table S6 and Supplementary Table S6b report the clinical association and exploratory analyses, and Supplementary Table S7 gives the region-by-age interaction tests. Supplementary Fig. S1 schematises the EEG network construction and the four graph-theoretic indices. All supplementary tables and figures are cited by number in the main text.

References

Achenbach TM, Rescorla LA (2001) Manual for the ASEBA school-age forms & profiles. University of Vermont, Research Center for Children, Youth, & Families, Burlington, VT

Alexander LM, Escalera J, Ai L, et al (2017) An open resource for transdiagnostic research in pediatric mental health and learning disorders. Scientific Data 4:170181. https://doi.org/10.1038/sdata.2017.181

Benjamini Y, Hochberg Y (1995) Controlling the false discovery rate: A practical and powerful approach to multiple testing. Journal of the Royal Statistical Society: Series B 57:289–300. https://doi.org/10.1111/j.2517-6161.1995.tb02031.x

Bullmore E, Sporns O (2009) Complex brain networks: Graph theoretical analysis of structural and functional systems. Nature Reviews Neuroscience 10:186–198. https://doi.org/10.1038/nrn2575

Casey BJ, Jones RM, Hare TA (2008) The adolescent brain. Annals of the New York Academy of Sciences 1124:111–126. https://doi.org/10.1196/annals.1440.010

Caspi A, Moffitt TE (2018) All for one and one for all: Mental disorders in one dimension. American Journal of Psychiatry 175:831–844. https://doi.org/10.1176/appi.ajp.2018.17121383

Gao W, Lin W, Grewen K, Gilmore JH (2017) Functional connectivity of the infant human brain: Plastic and modifiable. The Neuroscientist 23:169–184. https://doi.org/10.1177/1073858416635986

Gogtay N, Giedd JN, Lusk L, et al (2004) Dynamic mapping of human cortical development during childhood through early adulthood. Proceedings of the National Academy of Sciences 101:8174–8179. https://doi.org/10.1073/pnas.0402680101

Gorgolewski KJ, Auer T, Calhoun VD, et al (2016) The brain imaging data structure, a format for organizing and describing outputs of neuroimaging experiments. Scientific Data 3:160044. https://doi.org/10.1038/sdata.2016.44

Gramfort A, Luessi M, Larson E, et al (2013) MEG and EEG data analysis with MNE-Python. Frontiers in Neuroscience 7:267. https://doi.org/10.3389/fnins.2013.00267

Hagberg AA, Schult DA, Swart PJ (2008) Exploring network structure, dynamics, and function using NetworkX. Proceedings of the 7th Python in Science Conference 11–15

Humphries MD, Gurney K (2008) Network “small-world-ness”: A quantitative method for determining canonical network equivalence. PLOS ONE 3:e2051. https://doi.org/10.1371/journal.pone.0002051

Hunter JD (2007) Matplotlib: A 2D graphics environment. Computing in Science & Engineering 9:90–95. https://doi.org/10.1109/MCSE.2007.55

Huxley JS (1932) Problems of relative growth. Methuen & Co., London

Insel TR, Cuthbert BN (2009) Endophenotypes: Bridging genomic complexity and disorder heterogeneity. Biological Psychiatry 66:988–989. https://doi.org/10.1016/j.biopsych.2009.10.008

Latora V, Marchiori M (2001) Efficient behavior of small-world networks. Physical Review Letters 87:198701. https://doi.org/10.1103/PhysRevLett.87.198701

Ledoit O, Wolf M (2004) A well-conditioned estimator for large-dimensional covariance matrices. Journal of Multivariate Analysis 88:365–411. https://doi.org/10.1016/S0047-259X(03)00096-4

Maslov S, Sneppen K (2002) Specificity and stability in topology of protein networks. Science 296:910–913. https://doi.org/10.1126/science.1065103

Newman MEJ, Girvan M (2004) Finding and evaluating community structure in networks. Physical Review E 69:026113. https://doi.org/10.1103/PhysRevE.69.026113

Nunez PL, Srinivasan R (2006) Electric fields of the brain: The neurophysics of EEG, 2nd edn. Oxford University Press, New York

Opsahl T, Agneessens F, Skvoretz J (2010) Node centrality in weighted networks: Generalizing degree and shortest paths. Social Networks 32:245–251. https://doi.org/10.1016/j.socnet.2010.03.006

Pedregosa F, Varoquaux G, Gramfort A, et al (2011) Scikit-learn: Machine learning in Python. Journal of Machine Learning Research 12:2825–2830

Power JD, Cohen AL, Nelson SM, et al (2011) Functional network organization of the human brain. Neuron 72:665–678. https://doi.org/10.1016/j.neuron.2011.09.006

Rubinov M, Sporns O (2010) Complex network measures of brain connectivity: Uses and interpretations. NeuroImage 52:1059–1069. https://doi.org/10.1016/j.neuroimage.2009.10.003

Saramäki J, Kivelä M, Onnela J-P, et al (2007) Generalizations of the clustering coefficient to weighted complex networks. Physical Review E 75:027105. https://doi.org/10.1103/PhysRevE.75.027105

Shaw P, Kabani NJ, Lerch JP, et al (2008) Neurodevelopmental trajectories of the human cerebral cortex. The Journal of Neuroscience 28:3586–3594. https://doi.org/10.1523/JNEUROSCI.5309-07.2008

Shirazi SY, Franco A, Hoffmann MS, et al (2024) HBN-EEG: The FAIR implementation of the Healthy Brain Network (HBN) electroencephalography dataset. bioRxiv. https://doi.org/10.1101/2024.10.03.615261

Smit DJA, Geus EJC de, Nieuwenhuijzen ME van de, et al (2011) Scale-free modulation of resting-state neuronal oscillations reflects prolonged brain maturation in humans. The Journal of Neuroscience 31:13128–13136. https://doi.org/10.1523/JNEUROSCI.1678-11.2011

Vértès PE, Bullmore ET (2015) Annual research review: Growth connectomics—the organization and reorganization of brain networks during normal and abnormal development. Journal of Child Psychology and Psychiatry 56:299–320. https://doi.org/10.1111/jcpp.12365

Virtanen P, Gommers R, Oliphant TE, et al (2020) SciPy 1.0: Fundamental algorithms for scientific computing in Python. Nature Methods 17:261–272. https://doi.org/10.1038/s41592-019-0686-2

West GB, Brown JH, Enquist BJ (1997) A general model for the origin of allometric scaling laws in biology. Science 276:122–126. https://doi.org/10.1126/science.276.5309.122

Whitaker KJ, Vértès PE, Romero-Garcia R, et al (2016) Adolescence is associated with genomically patterned consolidation of the hubs of the human brain connectome. Proceedings of the National Academy of Sciences 113:9105–9110. https://doi.org/10.1073/pnas.1601745113

Whitford TJ, Rennie CJ, Grieve SM, et al (2007) Brain maturation in adolescence: Concurrent changes in neuroanatomy and neurophysiology. Human Brain Mapping 28:228–237. https://doi.org/10.1002/hbm.20273

Zhang K, Sejnowski TJ (2000) A universal scaling law between gray matter and white matter of cerebral cortex. Proceedings of the National Academy of Sciences 97:5621–5626. https://doi.org/10.1073/pnas.090504197

Supplementary Files

This is a list of supplementary files associated with this preprint. Click to download.

- Supplementarymaterial.docx